Nuclear Engineering and Technology 58 (2026) 103934

Contents lists available at ScienceDirect

Nuclear Engineering and Technology

journal homepage: www.elsevier.com/locate/net

Original Article

Impact of oscilloscope connections and bandwidth on signal formation from a SiPM coupled to a LYSO scintillator for gamma spectroscopy

Marcelo Bender Perotoni [a,*], Georgious Konstantinou [b], Adelson Duarte dos Santos [c], Daniel Alexandre Baptista Bonifacio [c]

[a] Universidade Federal do ABC (UFABC), Santo André, SP, Brazil
[b] École Polytechnique Fédérale de Lausanne, Neuchâtel, Switzerland
[c] Instituto de Pesquisas Energéticas Nucleares (IPEN), São Paulo, São Paulo, Brazil

ARTICLE INFO

Keywords:
Analogue electronic circuits
Front-end electronics for detector readout
Instrumentation and methods for gamma spectroscopy

ABSTRACT

This article explores the signal produced by a silicon photomultiplier (SiPM) coupled to a LYSO scintillator in gamma spectroscopy using time and frequency-domain measurements with an oscilloscop. Analyses were performed to address the influence of coaxial cables and oscilloscope probes in the measurements. Limitations of the oscilloscopes bandwidth on the extracted pulses were studied, as well as investigation of the effect of the ambient disturbances, using the two types of cable connections. The analytic Fourier transform of the pulse is analyzed, to indentify the parameters correlating both time and frequency domain. Since there are no further additional amplifiers or signal conditioning stages after the sensor, the results represent the unfiltered signal shape collected by the oscilloscope input impedance. Conclusions are presented as guidelines and design trade-offs concerning the instrumentation and pre-amplifier design.

1. Introduction

The Silicon Photomultiplier (SiPM) is a cost-effective sensor for ultra-low light level detection down to individual optical photons [1,2]. It is employed in several applications [3], including scintillator-based gamma-ray measurements [4], and the probing of biological tissues with picosecond pulse lasers [5]. SiPMs are essentially a set of SPADs (single photon avalanche diodes) in parallel configuration, each one with its own quenching resistor, operating in Geiger mode, when biased above the breakdown voltage. The SiPM signal is the summation of the responses of the SPADs. Each SPAD contributes its single photon response, which builds up to produce the detectable scintillation pulse [6].

The emitted scintillation light is isotropic, and the SiPM is typically placed on one side of the scintillation volume, while the remaining surfaces are covered with reflective material to minimize light loss. As a result, the detected photons are either emitted directly toward the SiPM or reach it after undergoing reflections from other surfaces [7]. Additionally, light extraction is challenging due to the generally high refractive index of scintillators, which exceeds 2 in materials such as Bismuth Germanate (BGO) [8]. Even when coupling materials like optical grease are used, the extraction angle within the crystal remains limited to approximately 20° [9].

Taking into account the time-dependent behavior of photon emission, travel time in a high refractive index material, and extraction, the already decimated scintillation light is eventually extracted from the crystal and enters the top surface of the SiPM, usually also coated with a quartz or epoxy resin layer [10] for protection. The SiPM also has a finite capability to detect photons, mainly driven by the quantum efficiency of the material and the sensitive surface as a percentage of the detector surface [11]. The product of these two factors and the avalanche triggering probability gives the photon detection efficiency (PDE), which is a wavelength-dependent benchmark for evaluating how well the SiPM can detect light across the emission spectrum of a given source. Common detectors peak around 420 nm with a PDE of up to 50 %, while other designs focus on the vacuum ultraviolet regions (VUV) area and also in the infra-red range, with applications in Light Detection and Ranging (LIDAR). Recent advances claim even higher PDE values [12].

Although the exact SPAD design varies between different models, there are some common characteristics. The microcell pitch is typically between 20 μm and 100 μm [13]. They usually have a top absorber layer, a few micrometers thick, where photons are received, ionizing silicon atoms and producing electron-hole pairs. Due to the high field

* Corresponding author.
E-mail address: mperoconsult@gmail.com (M.B. Perotoni).

https://doi.org/10.1016/j.net.2025.103934
Received 16 April 2025; Received in revised form 20 August 2025; Accepted 22 September 2025
Available online 23 September 2025

amplitude inside the silicon, caused by the reverse bias, these pairs are accelerated and induce similar ionization in the avalanche multiplication/depletion region and towards the PN junction. The avalanche multiplication process is self-sustaining until the current is quenched. Each SPAD in the SiPM has a quenching resistor, so that they operate indepently [2]. Electrodes are used to extract this single-photon avalanche current pulse to the external circuitry.

The recharge of the SPAD through the quenching resistor typically takes tens of nanoseconds [14]. At the same time, depending on factors such as the value of the reverse bias voltage and the device temperature, the intrinsic electron kinetics of silicon might cause self-triggering of the avalanche mechanism without an external trigger, producing a dark current [15].

In this sense, the scintillation pulse, as received by the data acquisition system, is the convolution of the SPAD response and the scintillator light emission, with the addition of the different spurious mechanisms described above.

Particularly for highly luminous materials such as LYSO:Ce (Lutetium Yttrium Orthosilicate), a large number of SPADs get triggered due to the detection of primary and secondary phtotons [16]. This type of SiPM saturation becomes dominant for small detector designs with pixel areas such as 1×1 mm^2 or for designs with very large area SPADs, along with other factors such as the PDE, which is function of the bias voltage, and also the fill factor (FF) of the individual SPAD.

For gamma-ray energy and time determination using scintillators, investigations on the proper amplifier design after the sensor have been actively reported, using approaches such as common base amplifiers [17], which take advantage of their inherent extended upper frequency limit because they are not subject to the Miller effect. Their implementation using CMOS technology [18] was also reported. Amplifier power consumption is a relevant factor, and it is addressed by using wideband microwave monolithic integrated circuits (MMICs) together with balun transformers [19]. In a previous work [20], an off-the-shelf RF MMIC was compared against a common emitter transistor amplifier, with the former providing better results at the expense of a larger current consumption. The sensor's large capacitance also imposes a severe constraint on the amplifier design, as it impacts the way either slow or fast components of the double-exponential pulse are processed. Three different amplifier topologies were analyzed with a view towards timing readout in SiPMs [21], showing the correlation between these three designs and their corresponding overall timing performance.

Recently, advances in the use of metallic trenches in the SiPM sensor structure enable a more packed array, since they decrease the level of optical crosstalk, increasing the efficiency and output amplitude levels of the SiPM [22]. These higher pulse voltages eventually might make preamplification unnecessary, with only a buffering stage before the analog acquisition or an analog-to-digital conversion.

The motivation for this article is the measurement of the SiPM pulse without signal conditioning or unwanted filtering made by finite bandwidth amplifiers stages so that we can measure and analyze the unfiltered SiPM signal. It covers the experimental test setup of a commercial SiPM, and its interaction with the oscilloscope, which aims to capture the pulse with the best signal-to-noise ratio. Though the observed results were particular for the used LYSO-SiPM pair, the conclusions and trends are general for other similar hardware setups. A single SiPM was used to focus the analysis onto the instrumentation setup, discarding differences in rise-time and frequency contents in case different commercial SiPMs were used. The sensor capacitance was estimated based on these measurements, without any curve fitting procedure, which enables an optimal preamplifier design. Conclusions are drawn based on the experiments, which guide further laboratory setups involving the use and testing of SiPMs.

2. Circuit detector and basic concepts

The SiPM used was the Broadcom AFBR-S4N44C013, with a sensitive area of 3.72×3.72 mm^2 and a cell pitch of 30×30 μm^2, optimized for the blue and near UV (ultraviolet) region [2]. Its PDE is 55 % at 420 nm. A SiPM with a smaller area would, however, generate pulses with steeper transient pulses, reaching higher frequencies. The SiPM was optically coupled to a LYSO scintillation crystal (cuboid with dimensions 4 x 4 x 4 mm^3) using a Visilox V788 optical grease. LYSO possesses intrinsic radioactivity due to the presence of Lu-176. This radioactivity level is sufficient to produce scintillation light, which is collected by the SiPM, the number of electrons related to the incoming photons expressed by the PDE parameter. The process forms a double exponential shaped pulse, so there was not any other source of radiation but the LYSO and the ambient itself. Fig. 1 shows the arrangement of the two situations, alongside the SiPM carrier board. The SiPM's nominal breakdown voltage is 26.9 V, so a 30–31 V bias voltage was set throughout. The SiPM was mounted onto an in-house designed printed circuit board (PCB) with only passive components, as shown in Fig. 2. R4 and C1 operate as a low-pass filter for the DC bias (cutoff frequency of 4.8 kHz). Instead of a single-ended AC output point, a differential approach was used, following [23], where the 50 Ω resistor and a capacitor, not shown in the diagram and only used for differential measurements, separate the AC part from the DC biasing power. This resistor value matches the standard reference impedance in RF instrumentation and coaxial cables, minimizing reflections arising from mismatches. The board has SMA coaxial connectors to provide access to signals, as well as pins to be connected to the oscilloscope probe tip.

The typical SiPM current waveform has a format similar to Ref. [24]:

$$i(t) \approx i_o\left(e^{\frac{-t}{\tau_d}} - e^{\frac{-t}{\tau_r}}\right). \tag{1}$$

where τ_d and τ_r are the decay and rise time constants, respectively, with the latter in the nanosecond range and the former ranging from nanoseconds to microseconds. Physically, these time constants are related to the resistors and capacitors that model the sensor; further details are covered elsewhere [2]. Integrating the current pulse over time results in the total charge transferred between the sensor terminals. Besides the SiPM, τ_r also increases with the scintillator path length, as this event is derived from multiple interactions, such as Compton scattering [24]. The Fourier Transform of the current for $t \geq 0$ can be written as:

$$I(\omega) \approx i_o\left[\frac{1}{j\omega + \frac{1}{\tau_d}} - \frac{1}{j\omega + \frac{1}{\tau_r}}\right] \tag{2}$$

with ω representing the angular frequency variable. This expression, taken only its amplitude results in:

$$|I(\omega)| \approx \frac{\left|\left(\frac{1}{\tau_r}\right) - \left(\frac{1}{\tau_d}\right)\right|}{\left|j\omega + \left(\frac{1}{\tau_r}\right)\right|\left|j\omega + \left(\frac{1}{\tau_d}\right)\right|} = \frac{\left|\left(\frac{1}{\tau_r}\right) - \left(\frac{1}{\tau_d}\right)\right|}{\sqrt{\left(\omega^2 + \frac{1}{\tau_r}\right)}\sqrt{\left(\omega^2 + \frac{1}{\tau_r}\right)}} \tag{3}$$

whose magnitude in dB can be expressed as:

$$|I(\omega)| \approx 20\,log\left|\frac{1}{\tau_r} - \frac{1}{\tau_d}\right| - \left[10\,log\left(\omega^2 + \frac{1}{\tau_r^2}\right) + 10\,log\left(\omega^2 + \frac{1}{\tau_d^2}\right)\right] \tag{4}$$

The first term is equivalent to a DC energy, and the remaining two components inside the brackets impose the low-pass characteristic of the energy, with breaking points at frequencies $1/(2\pi\tau_r)$ and $1/(2\pi\tau_d)$. Since τ_r is generally smaller than τ_d, the pulse energy starts falling after $1/(2\pi\tau_d)$, with a slope of −20 dB/decade and it falls further (−40 dB/dec) when the frequency reaches $1/(2\pi\tau_r)$ [25].

In terms of applications, two kinds of parameters of interest are extracted from the waveform: energy, inferred by the pulse height, and timing, which relies on the fast component of the waveform, such as when the leading-edge timing is applied. Therefore, whereas signal-to-

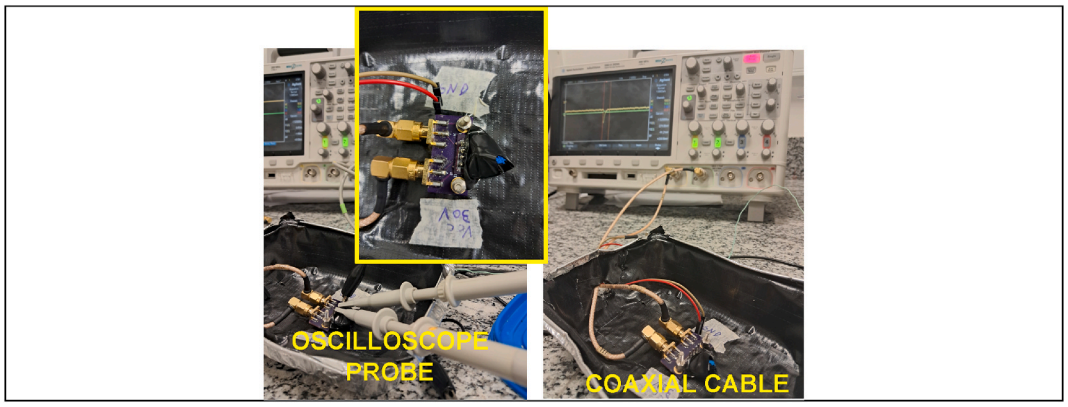

Fig. 1. Setup with the oscilloscope probe and coaxial cable. In detail, the carrier board with the scintillator covered with black tape.

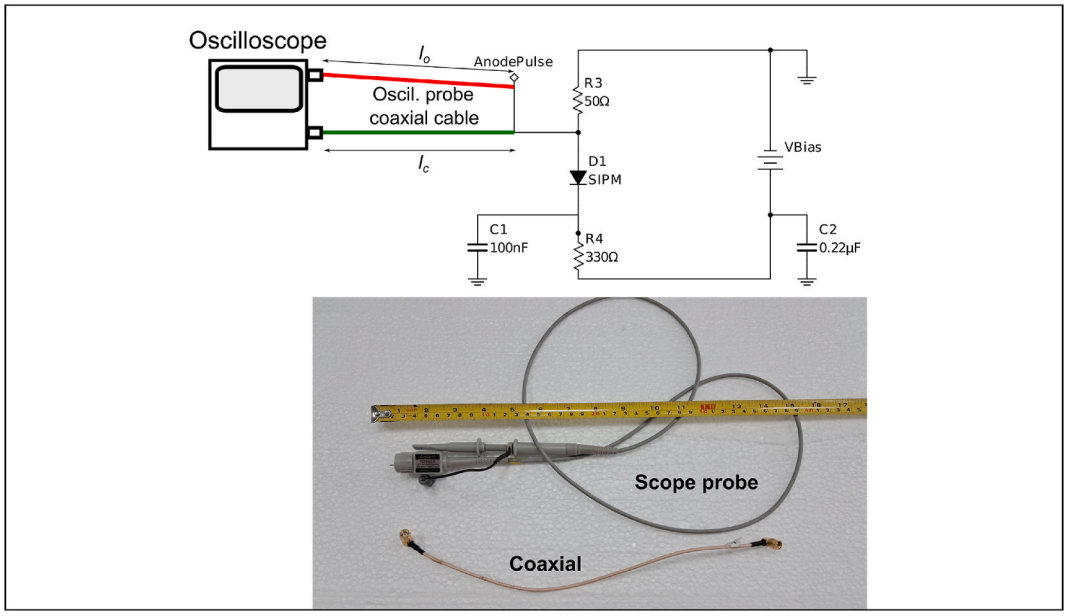

Fig. 2. SIPM board schematic and the probe ($l_o = 116$ cm) and coaxial cable ($l_c = 34$ cm). The coaxial cable (green trace) and oscilloscope probe (red trace) each go to a respective scope channel.

noise amplitude is important for energy measurements, slope-to-noise ratio is fundamental for timing. Thus, for timing, both amplifiers and detectors should have similar bandwidths [24]. Hence, a good estimate of the average pulse received by the sensor is of paramount importance to continue with an optimal circuit and system design.

3. Influence of the cable on the time and frequency domain pulse response

The first test investigates how the use of a coaxial cable and the oscilloscope probe impacts the pulse waveform generation. A 200-MHz Agilent Infinii DSO-X 2024A oscilloscope was employed. Its input impedance is 1 MΩ in parallel with an 11 pF capacitance. Also, its maximum 200-MHz bandwidth demands a 10:1 voltage attenuation at the passive probe. A total of 177 pulses were acquired with both oscilloscope probes and with a coaxial probe, connected to the SMA outputs, using the same SiPM circuit. Fig. 3 shows two sampled waveforms, extracted from the measured set using the aforementioned setup and bias voltages.

Visually, the results show that the coaxial cable induces less noise in the waveform. The less noisy trace is due to the electromagnetic shielding of the coaxial cable and the SMA connector when contrasted with the unshielded probe tip. Also, the frequency domain representation of both curves shows that acquiring the pulses with the oscilloscope resulted in a smaller immunity against stray electromagnetic interference (EMI) picked up from the environment, particularly at the frequencies of 82 MHz and 125 MHz. For 82 MHz, the oscilloscope cable picked up this stray 31 dB below the maximum 0 dB observed at zero-frequency, whereas for the coaxial cable, its amplitude was 61 dB below, a 30 dB difference. For 125 MHz, the same 30 dB difference was observed; −47 dB for the oscilloscope and −77 dB for the coaxial. It is possible to see that the pulse energy for this particular SiPM falls about 35 dB of its peak around 10 MHz. In case the SiPM pulse reaches frequencies within the areas where the EMI arises, the waveform would be compromised, resulting in imprecise energy readings.

The signal-to-noise ratio (SNR)parameter can be computed for the curves, whose samples are s_n, and is defined here as:

$$SNR = \frac{P_{noise} + P_{signal}}{P_{noise}} = \frac{\sum_{n=0}^{t_r} |s_n|^2}{\sum_{n=t_r+1}^{2t_r} |s_n|^2} \tag{5}$$

The definition considers the numerator as the sum of both signal and noise since it is not possible to have a real-world noiseless signal. P_{signal}

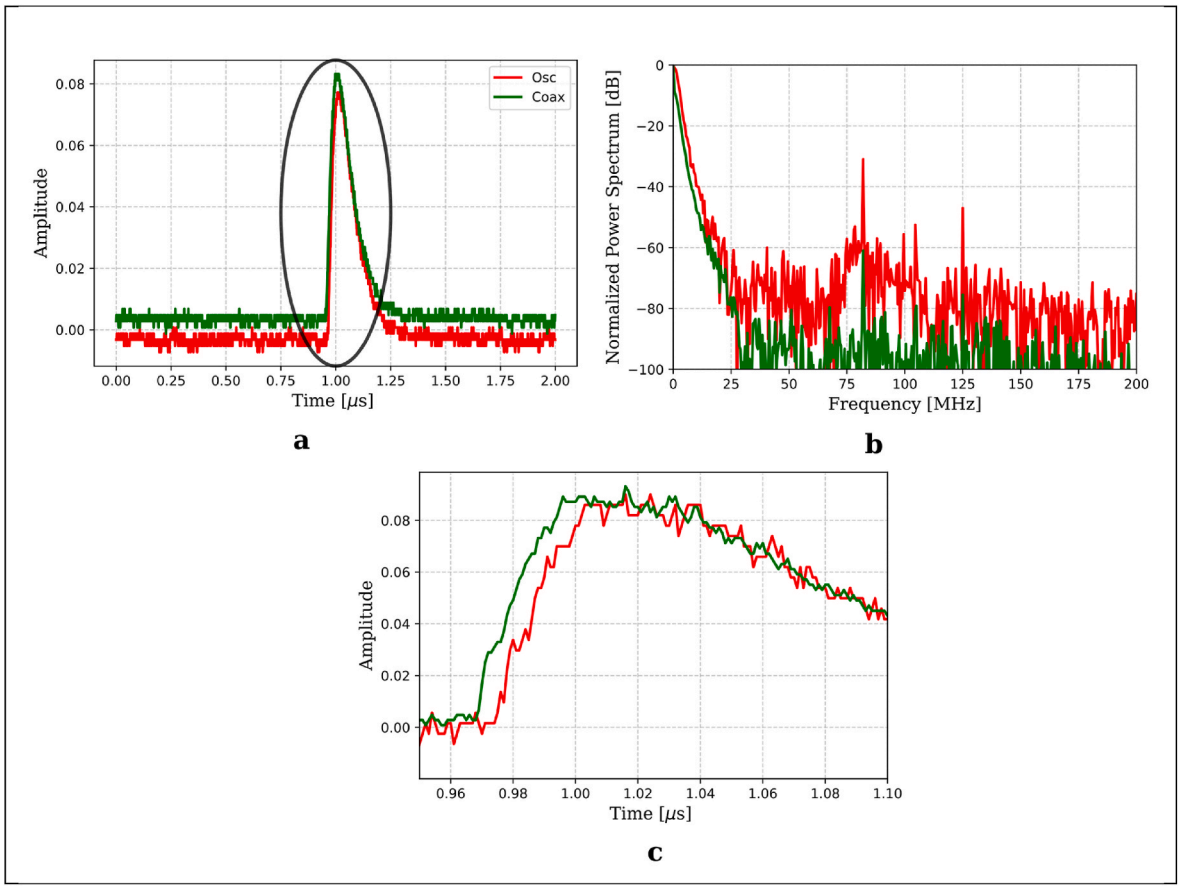

Fig. 3. Two individual pulses acquired with the oscilloscope probe and coaxial cable, in time (a) and frequency (b) domains. In (c) a magnified view of the rise time region is shown.

and P_{noise} are the signal and noise power, respectively, and t_r is the index associated to a moment just before the pulse onset, set by the user and dependent on the oscilloscope horizontal (time) setting. In the case of the curves shown in Fig. 3, a value of 0.9 ns was used, meaning that the segment before that threshold was considered to be made of pure noise and afterwards, signal contaminated with noise. This 0.9 ns limit was found to be constant among all the acquired samples. Table 1 contains the SNR of the ensemble of 177 acquired pulses.

A difference of 0.38 dB was observed in the averages of SNR within the ensembles, in favor of the coaxial cable. In addition, the higher standard deviation of the oscilloscope-acquired waveforms shows a larger variability imposed by the instrument. Fig. 4 shows the histogram of the complete set of measurements. The plot shows a slightly larger concentration of points of the coaxial cable measurements at the largest SNR part of the plot.

4. Coaxial cable vs. oscilloscope probe - EMC test

To address the shielding capacity of the coaxial cable in contrast to the oscilloscope probe, the following setup was used, shown in Fig. 5. An equal-length sector of both cables was exposed to a radiated electromagnetic field emitted by a coil with 9.6 cm diameter. The coil was fed by an RF signal generator followed by a 30-dB power amplifier (maximum frequency 500 MHz). Since the overall length of the oscilloscope probe is longer than the coaxial length, metallic shielding was used to enforce the same area subjected to illumination. The oscilloscope probe was left under the metallic plate, given its higher sensitivity caused by open ends, without any kind of shield. The oscilloscope had a 200-MHz bandwidth. Both ends were terminated with 50 Ω resistors. A previous calibration was used to ensure that the acquired voltage amplitudes were the same when using the same input signal for both oscilloscope inputs.

The parameter *SE*, shielding effectiveness, was defined as:

$$SE = 20\ log \frac{V_{scope}}{V_{coax}}\ [dB] \tag{6}$$

The parameter *SE* indicates the amount of shielding, in decibels, provided by the coax compared to the probe.

From the results, one can see that in the worst case, observed at 90 MHz, the coaxial cable provided above 15 dB of shielding against radiated fields in comparison to the oscilloscope case.

Table 1
Statistics of the measured SNR [dB].

	Oscilloscope	Coaxial
Average	19.70	20.08
Std. deviation	2.93	2.61

5. Coaxial cable vs. oscilloscope probe - simulation

The oscilloscope probe is optimized for minimizing reflections due to its internal lossy transmission line [26]. That is not the case for a good quality coaxial cable, which is expected to have a low loss. Therefore, in terms of overall immunity against mismatch reflections showing up as ringing in the pulse waveform, the oscilloscope probe potentially has a better performance. That was not observed in the experiments because the pulse frequency content was reasonably low, but in case the SiPM delivers a signal whose energy extends above 100 MHz, reflections from the coaxial cable mismatch might be an issue. Also, in this experiment,

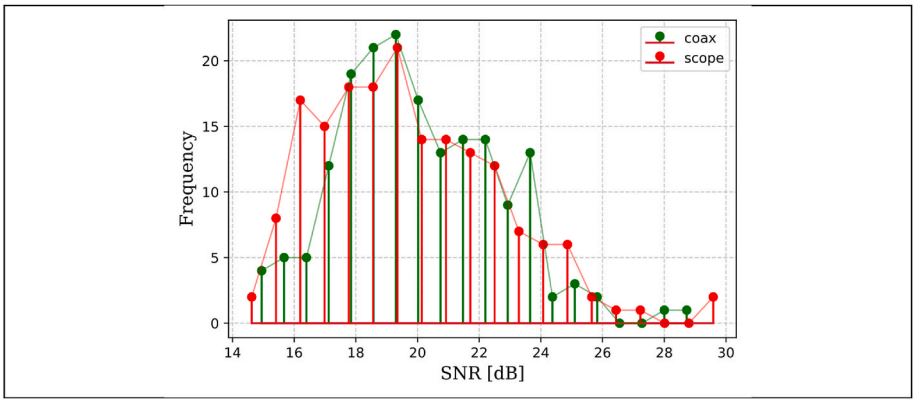

Fig. 4. Histogram of the 177 acquired pulses simultaneously acquired with the coaxial and oscilloscope probe.

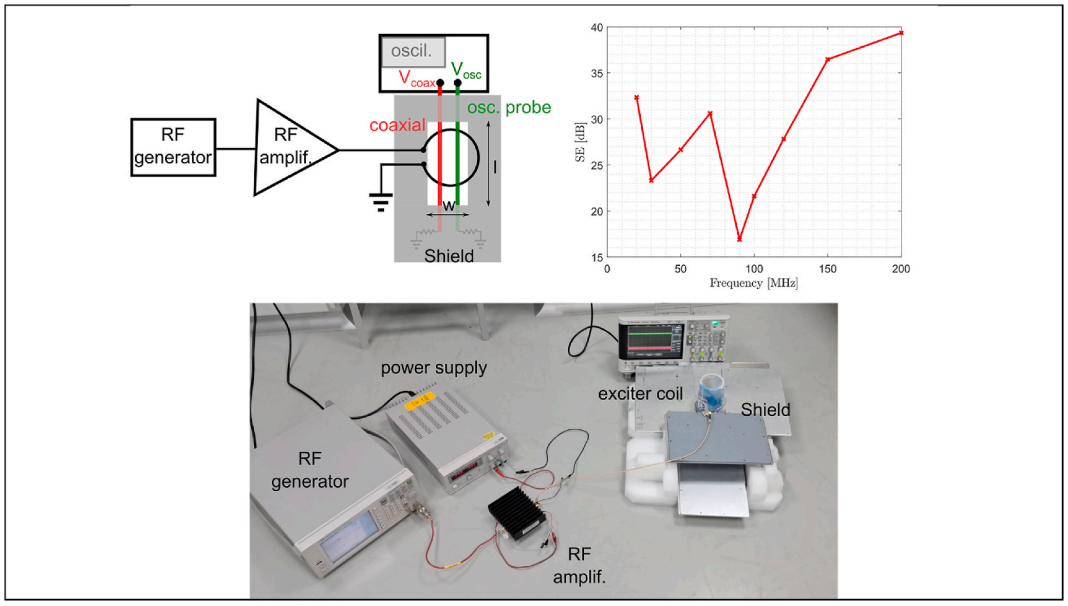

Fig. 5. Used SE test setup, block diagram and actual arrangement and respective results.

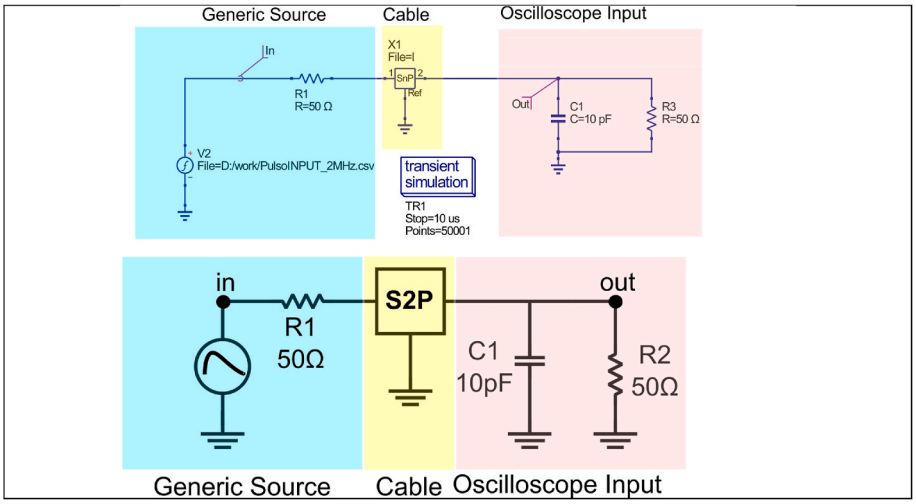

Fig. 6. Electrical model of a generic voltage source connected to an oscilloscope with a coaxial cable.

the source (SiPM) was deliberately set to be around 50 Ω, so the reflections are naturally minimized.

Other points of concern regarding the oscilloscope probe are the tip and the ground clip. They represent an inductance and might be cumbersome for fast signals, defined as when the circuit lengths are equal or larger than a tenth of the wavelength in question, meaning that phase effects start to arise and should be considered. For discrete electronics, signals begin to be considered fast (or RF) for about 10 MHz, where the inductances, capacitances, and circuit physical lengths start to impose phase differences when the signals are observed on various circuit points. Associated with other distributed capacitive reactances, these inductances might excite resonances in the signal. The use of a coaxial connector, such as of BNC or SMA type, connecting to a coaxial cable, eliminates this issue.

Coaxial cables, however, present a capacitance to the system, and it has to be taken into account. The used cables had approximately 30 cm, so it results in 30 pF considering the typical RG 58 capacitance (100 pF/m), which has the effect as a distributed capacitance along the cable length.

Taking into account the circuit shown in Fig. 6, R1 represents the source impedance and the oscilloscope is represented by R2 in parallel with C1, set to 10 pF. The cable was measured in a Vector Network Analyzer, and its scattering parameters were imported into the circuit simulation using the Touchstone (S2p) file. It is an electrical model of the used setup, with the voltage source representing not the SiPM, but the signal it generates. To address the effect of it with two different pulses, follow Eq. (1) with the parameters according to Table 2.

The relation between rise time tr and bandwidth BW was employed [27]:

$$BW \approx \frac{k}{t_r} \tag{7}$$

The parameter $k = 0.338$ is used for gaussian pulses, which approximates better to the double-exponentials here applied than that most common $k = 0.35$, better suit for single-pole exponential decays responses to step inputs. It guarantees, for the case of a double exponential, a 34 dB drop at its BW, in contrast to the maximum energy, observed at DC.

The circuit was simulated for the two signals, results are shown in both time and frequency domains in Fig. 7.

From the simulation results, the hundredfold distance in rise time for the pulse frequencies, albeit keeping the same waveform, generates quite different responses. The 2-MHz s_1 output pulse spectrum follows its input up to a decade above 2 MHz, whereas s_2 has a 0.3 dB drop in the output energy at the 200 MHz theoretical break point, a rather small difference due to the short cable that was used, on purpose to preserve the signal integrity. The capacitance associated with the coaxial cable might impose a toll on fast signals, with loss in the leading edge which conveys timing information.

Table 3 contains the time distance between output and input peaks, as well as their linear amplitude attenuation. s_1 output is 5 ns ahead of the input, showing the derivative (high-pass filter) effect the circuit imposes, whereas s_2 output is delayed by 2.24 ns. From the viewpoint of attenuation, not much difference is observed. Much more impact on the attenuation is caused when the source resistance (R1) is increased, which for the SiPM case is, in any case, undesirable due to the effect it creates on the pulse rise time.

Table 2
Pulse parameters.

Signal	Bandwidth [MHz]	t_r [ns]	t_d [ns]
s_1	$BW_1 = 2$	$t_{r1} = 175$	$t_{d1} = 10t_{r1}$
s_2	$BW_2 = 200$	$t_{r2} = 1.75$	$t_{d2} = 10t_{r2}$

6. Comparison with a high-bandwidth oscilloscope

A 3-GHz oscilloscope (Rigol MSO8304A) was used with the same SiPM launch board. Measurements were carried out to compare it with the lower-frequency Agilent instrument, to investigate whether its much larger bandwidth (3 GHz versus 200 MHz) offered any relevant benefit. In addition to its larger bandwidth, it admits a 50 Ω input (capacitance 19 pF), which was used through-out the test. The 200 MHz instrument had a connection to a coaxial cable utilizing a BNC to SMA adapter, however, but its probe impedance was only allowed to be 1 MΩ. From the viewpoint of preserving the pulse shape, a smaller input resistance connected to the SiPM is more convenient in case of overlapping successive events [28], the so-called pile-up effect. Also, in case pulse pile-up takes place, the energy resolution is degraded. However, pile-up events are rare in our setup since Lu-176 activity is very low.

A comparison was performed using a setup (Fig. 8), where the same pulse output was acquired by both instruments. For that, only one SiPM output was used, and it was divided into each instrument. Given that there was only one available divider, the comparison was not carried out with the differential signal, which otherwise would require twice as many dividers and cables. Nonetheless, the scheme allows observing the actual difference of a much larger bandwidth instrument for this specific SiPM.

For the sake of comparison, Fig. 9 shows the results of two curves, representing events measured with both oscilloscopes. Results are shown normalized to their respective maximum amplitudes.

The 3 GHz bandwidth oscilloscope has a much noisier waveform when contrasted to the more modest instrument. That is explained by the noise amplitude formula:

$$V_n = \sqrt{4kTBR} \tag{8}$$

where V_n is the RMS noise voltage in Volts developed across a resistor of value R (unit: Ω) and measured with a bandwidth B (Hz) at Temperature T (Kelvin), and k is the Boltzmann's constant.

Concerning their power spectra, one can see that the DC content of both cases is not the same, difference ascribed to the 50 Ω input impedance of the 3 GHz scope in contrast to the 1 MΩ relative to the 200 MHz instrument. Also, the 3 GHz unit allows a much better sampling in contrast to the 200 MHz, resulting in a finer frequency resolution. Nevertheless, for this particular SiPM, the frequency content is not degraded by the more modest instrument. The tests indicate that an oscilloscope with a bandwidth much larger than that of the pulse might represent an overkill not only in terms of cost but also when the incoming noise is taken into account. It follows the common procedure of adding an RC (resistor-capacitor) low-pass filter just after the SiPM to artificially reduce the bandwidth and consequently the noise level [24].

7. Determining SiPM capacitance

Since the measurement is not carried out with any signal conditioning scheme, only the oscilloscope is left to be considered in the pulse response. From Eq. (1), the fast part (leading edge) of the pulse, which is controlled by the time constant τ_r, can be related to the SiPM electrical model as [3]:

$$\tau_r \approx RC_{HF} \tag{9}$$

where C_D is the micro-cell capacitance of the photo-diode, R_Q is the quenching resistance associated with its parasitic C_Q, and C_G is the overall capacitance associated with the routing interconnections. The delta function excites the cell that was hit by a photon, where there are $N-1$ unfired micro-cells. R_{IN}, in turn, accounts for the oscilloscope input in this case. Therefore, C_{HF} can be defined according to the elements shown in Fig. 10 as:

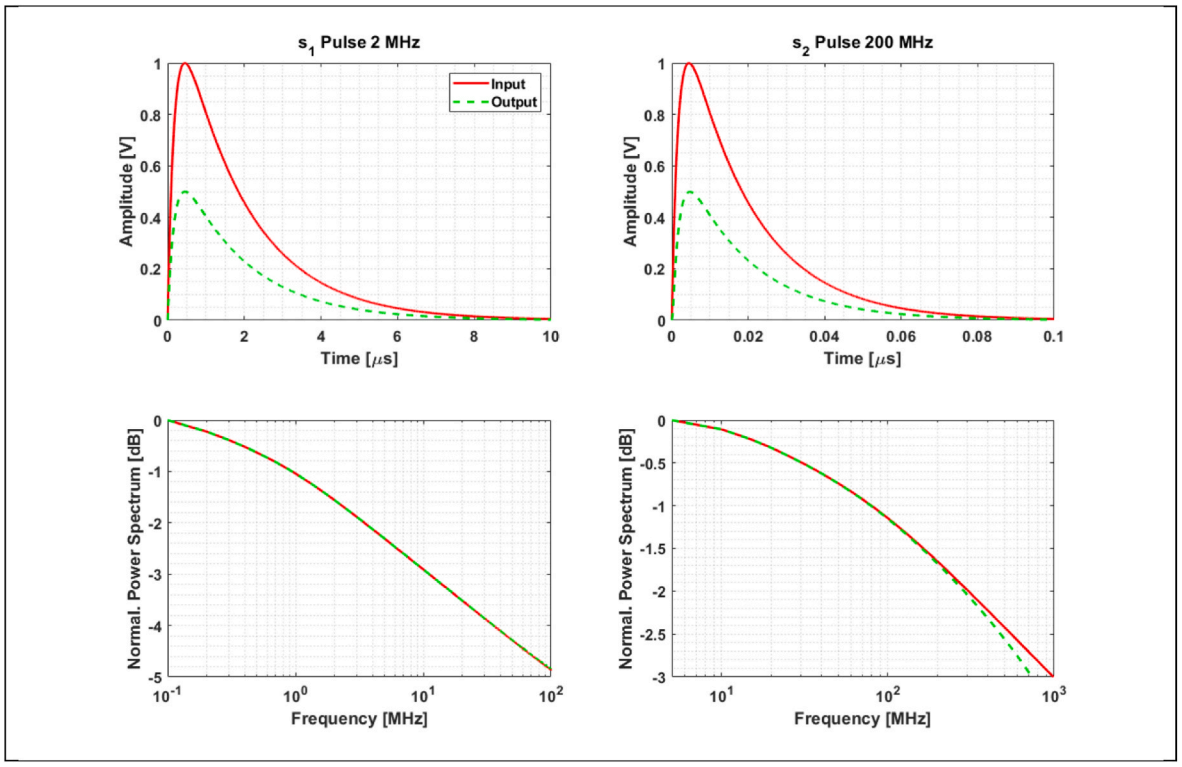

Fig. 7. Simulated pulses in time and frequency domains.

Table 3
Timing comparison.

signal	peak time diff. [ns]	peak amplit. att.
s_1 (2 MHz)	−5 (lead)	0.5
s_2 (200 MHz)	2.24 (delay)	0.48

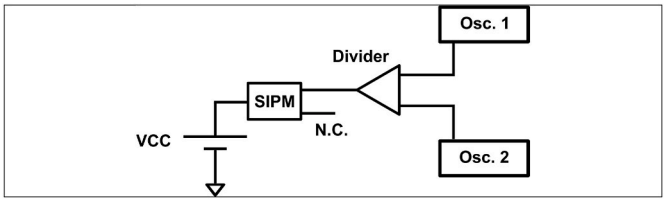

Fig. 8. Setup for two oscilloscopes acquiring the same pulse.

$$C_{HF} \approx C_G + N\frac{C_D C_Q}{C_D + C_Q} \tag{10}$$

A small C_Q implies a faster rise-time, whereas a larger quenching capacitance C_Q generates a higher-amplitude pulse, and if the design involves a larger SiPM area the C_G reduces the pulse in the time-domain amplitude while stretching its width in time [29]. C_{HF} represents the equivalent detector capacitance, which is of paramount importance for ensuring an adequate sensor circuit model in case of a computer simulation and also an optimized pre-amplifier design. In Ref. [30], the SiPM electrical model was found after fitting the measurements taken in two instruments, one LCR meter for 20 Hz to 2 MHz and a network analyzer for the range up to 500 MHz, into an analytical formula representing the input impedance variation in frequency. Another approach to fitting experimental data to a more complex electrical model used the diode I-V curve altogether with the time-domain pulse waveform, taken after the preamplifier [31]. A similar approach followed the CMOS SiPM array construction, where the measured and SPICE-simulated pulses were compared, alongside with other parameters extracted from laboratory tests, such as dark count rate, photon detection efficiency and crosstalk [32]. Instead of time-domain measurements, a vector network analyzer (VNA), model Rohde & Schwarz ZVB8, was used to fit the analytical SiPM input impedance with the scattering parameter S11 which represents the reflected wave only in the frequency domain. The SiPM was fed with a bias-T so that no DC energy was injected into the VNA [33], thereby isolating the AC and DC paths.

Here, for the sake of evaluation, the bandwidth-limited curve presented in Fig. 9 was fitted against the analytical formula Eq. (1), results shown in Fig. 10.

The fitted curve results in a $\tau_r = 3.7\text{E-}8$ s and $\tau_d = 1.6\text{E-}7$ s. From Eq. (9), considering $R_{IN} = 50\ \Omega$ in the oscilloscope results in a capacitance of 740 pF, which is close to the sensor datasheet (760 pF). Similarly, the low-frequency sensor capacitance C_{LF} can be estimated as:

$$C_{LF} \approx \frac{\tau_d - \tau_r}{R} \tag{11}$$

It is resulting in $C_{LF} = 2.46$ nF, which corresponds to the pulse trailing edge.

8. Conclusions

Some conclusions can be drawn from the experiment.

- The use of a coaxial cable instead of the oscilloscope probe showed better results even if the instrument does not offer the option of a channel with 50 Ω input impedance. The lower impedance of the coaxial cable also helps the pulse dynamics, particularly when there is an interest in the fast-leading edge.
- The use of a coaxial cable also showed better EMI immunity against noise, picked up from the environment, as measurements present in Table 1 demonstrated. A setup measurement addressed the difference in shielding between both coaxial and oscilloscope probes, with the latter showing immunity levels at least 15 dB larger in the range of 20 MHz–200 MHz.

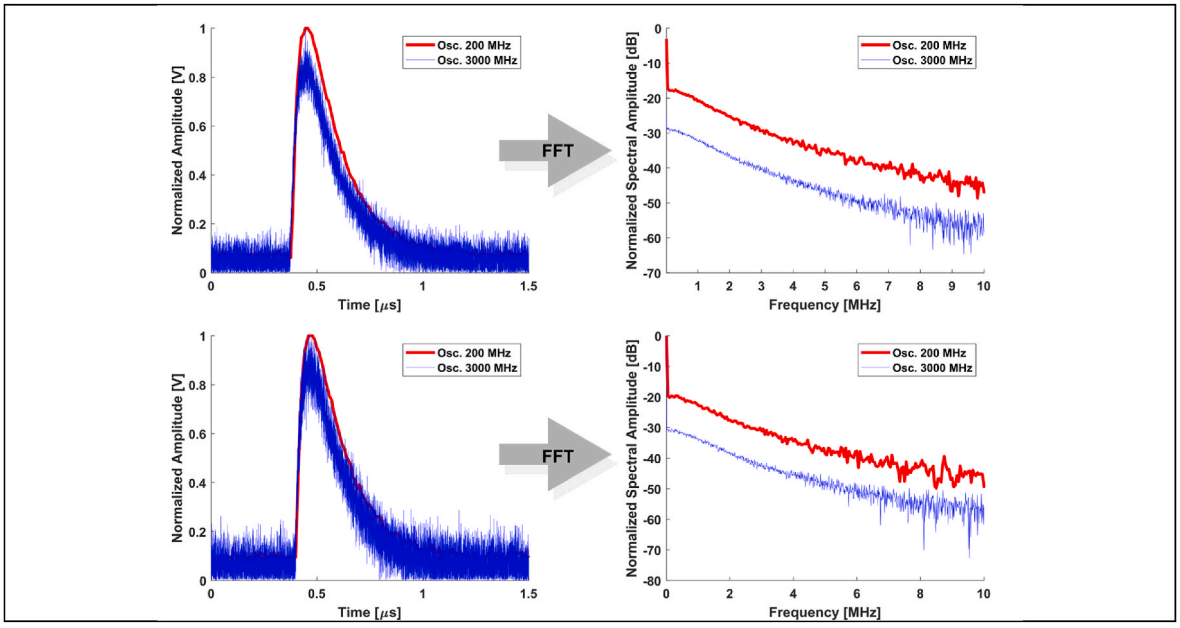

Fig. 9. Time and frequency content for two different pulses, simultaneously captured with both 200 MHz and 3000 MHz oscilloscopes.

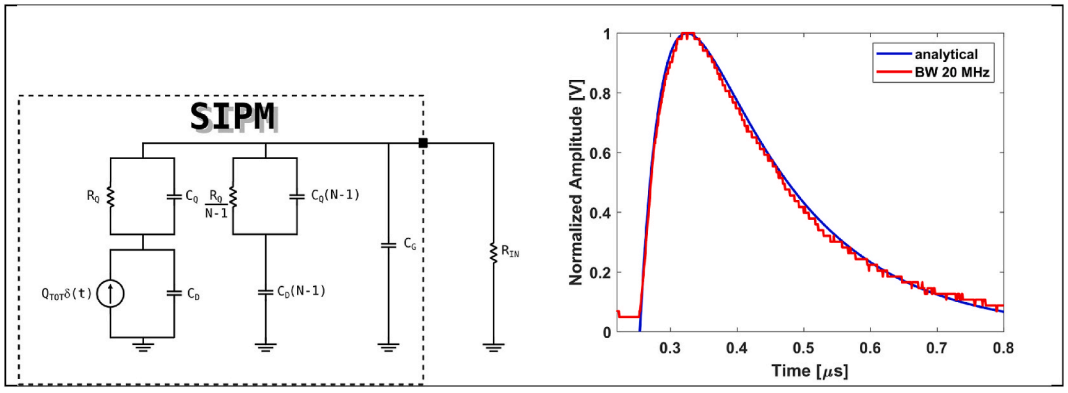

Fig. 10. SiPM electrical model (adapted from Ref. [3]) and fitted double exponential curve and the measurement.

- The coaxial cable capacitance might impose a restriction in terms of high-speed pulses, where this impedance might act as a low-pass filter on the SiPM pulse. There is therefore a trade-off between pulse integrity and noise immunity.
- The definition of the largest frequency content of the particular setting SiPM and radiation source is of paramount importance since it allows the use of an optimum instrumentation.Unfiltered signal measurement sensor enables the determination of its upper-frequency content. The same reasoning applies to the following low-noise amplifier that is connected to the SiPM, its bandwidth should not exceed the pulse frequency content limit in order to avoid increasing the noise level admitted into the system.
- Use of a too-large bandwidth oscilloscope degrades the signal-to-noise ratio of the pulse since the large bandwidth corresponds to larger noise amplitudes. The use of the reduced bandwidth channel option in the oscilloscope also showed good results when compared to the full-frequency range. The same reasoning applies to the pre-amplifier following the SiPM, an excessively large bandwidth has a risk of degrading the pulse signal-to-noise ratio.
- By analyzing the SiPM directly with an oscilloscope is possible to estimate the sensor capacitances, which enables a more suitable and customized design, which might include PCB parasitics and other items that are difficult to address unless a bench test is carried out.

CRediT authorship contribution statement

Marcelo Bender Perotoni: Writing – review & editing, Writing – original draft, Visualization, Supervision, Software, Resources, Project administration, Methodology, Investigation, Formal analysis, Data curation, Conceptualization. **Georgious Konstantinou:** Writing – review & editing, Writing – original draft, Visualization, Validation, Investigation. **Adelson Duarte dos Santos:** Writing – review & editing, Software, Resources, Methodology, Investigation. **Daniel Alexandre Baptista Bonifacio:** Writing – review & editing, Visualization, Supervision, Resources, Project administration, Investigation, Funding acquisition, Data curation.

Declaration of competing interest

The authors declare the following financial interests/personal relationships which may be considered as potential competing interests: None.

Acknowledgements

This work has been supported by the Brazilian funding agencies São Paulo Research Foundation (FAPESP, process Nos. 2020/13879-4 and

2023/00079-8), Conselho Nacional de Desenvolvimento Científico e Tecnológico (CNPq, grant agreements Nos. 202378/2020-9 and 435039/2018-0), Financiadora de Estudos e Projetos (FINEP, grant agreement No. 0294/16), and CAPES (Coordination for the Improvement of Higher Education Personnel). Their support is greatly acknowledged.

The authors gratefully acknowledge the IRD/CNEN for providing the point-like standard radioactive sources.

References

[1] K.S. Krane, D. Halliday, Introductory Nuclear Physics, Wiley, New York, 1987.
[2] F. Acerbi, S. Gundacker, Understanding and simulating SiPMs, Nucl. Instrum. Methods Phys. Res. 926 (2019) 16–35.
[3] P.P. Calò, F. Ciciriello, S. Petrignani, C. Marzocca, SiPM readout electronics, Nucl. Instrum. Methods Phys. Res. Sect. A Accel. Spectrom. Detect. Assoc. Equip. 926 (2019) 57–68.
[4] N. D'Ascenzo, V. Saveliev, Study of silicon photomultipliers for the medical imaging systems, Nucl. Instrum. Methods Phys. Res. A695 (2012) 265–267.
[5] A.D. Mora, L.D. Sieno, A. Behera, P. Taroni, D. Contini, A. Torricelli, A. Pifferi, The sipm revolution in time-domain diffuse optic, Nucl. Instrum. Methods Phys. Res. A978 (2020) 1–7.
[6] F. Zappa, S. Tisa, A. Tosi, S. Cova, Principles and features of single-photon avalanche diode arrays, Sensor Actuator Phys. 140 (2007) 103–112.
[7] P. Lecoq, Scintillation detectors for charged particles and photons, Particle Physics Reference Library: Volume 2: Detectors for Particles and Radiation 2 (2020) 45–89.
[8] M. Janecek, W.W. Moses, Measuring light reflectance of bgo crystal surfaces, IEEE Trans. Nucl. Sci. 55 (2008) 2443–2449.
[9] M. Salomoni, R. Pots, E. Auffray, P. Lecoq, Enhancing light extraction of inorganic scintillators using photonic crystals, Crystals 8 (2018) 1–35.
[10] I. Kochanek, Packaging strategies for large SiPM-based cryogenic photo-detectors, Nucl. Instrum. Methods Phys. Res. Sect. A Accel. Spectrom. Detect. Assoc. Equip. 980 (2020) 164487.
[11] G. Bonanno, P. Finocchiaro, A. Pappalardo, S. Billotta, L. Cosentino, M. Belluso, S. D. Mauro, G. Occhipinti, Precision measurements of photon detection efficiency for sipm detectors, Nucl. Instrum. Methods Phys. Res. Sect. A Accel. Spectrom. Detect. Assoc. Equip. 610 (2009) 93–97.
[12] F. Acerbi, G. Paternoster, S. Merzi, N. Zorzi, A. Gola, Nuv and vuv sensitive silicon photomultipliers technologies optimized for operation at cryogenic temperatures, Nucl. Instrum. Methods Phys. Res. Sect. A Accel. Spectrom. Detect. Assoc. Equip. 1046 (2023) 167683.
[13] D.P. Palubiak, M.J. Deen, Cmos spads: design issues and research challenges for detectors, circuits, and arrays, IEEE J. Sel. Top. Quant. Electron. 20 (2014) 6000718.
[14] D. Rideau, A. Oussaiti, R. Helleboid, G. Mugny, I. Nicholson, A. Bianchi, D. Golanski, B. Mamdy, J.-B. Kammerer, S. Rink, C. Lallement, B. Rae, W. Uhring, S. Pellegrini, M. Agnew, E. Lacombe, J.R. Manouvrier, M. Al-Rawhani, M, Single photon avalanche diode with Monte Carlo simulations: PDE, jitter and quench probability, in: 2021 International Conference on Simulation of Semiconductor Processes and Devices (SISPAD), 2021, pp. 1–4.
[15] D. Durini, C. Degenhardt, H. Rongen, A. Feoktystov, M. Schlösser, A. Palomino-Razo, H. Frielinghaus, S. van Waasen, Evaluation of the dark signal performance of different sipm-technologies under irradiation with cold neutrons, Nucl. Instrum. Methods Phys. Res. Sect. A Accel. Spectrom. Detect. Assoc. Equip. 835 (2016) 99–109.
[16] S. Gundacker, E. Auffray, N.D. Vara, B. Frisch, H. Hillemanns, P. Jarron, B. Lang, T. Meyer, S. Mosquera-Vazquez, P.L.E. Vauthey, Sipm time resolution: from single photon to saturation, Nucl. Instrum. Methods Phys. Res. Sect. A Accel. Spectrom. Detect. Assoc. Equip. 718 (2013) 569–572.
[17] J. Huizenga, S. Seifert, F. Schreuder, H. van Dam, P. Dendooven, H. Lohner, A fast preamplifier concept for SiPM-based time-of-flight PET detectors, Nucl. Instrum. Methods Phys. Res. 695 (2012) 379–384.
[18] L.B. Oliveira, C.M. Leitão, M.M. Silva, Noise performance of a regulated cascode transimpedance amplifier for radiation detectors, IEEE Trans. Circ. Syst. 59 (2012) 1841–1848.
[19] M. Krake, V. Nadig, V. Schulz, S. Gundacker, Power-efficient high- frequency readout concepts of SiPMs for TOF-PET and HEP, Nucl. Instrum. Methods Phys. Res. 1039 (2022) 1–6.
[20] C. Li, Y. Li, J. Xi, S. Xiang, K. Hu, Coincidence time resolution of radiation detector based on 6×6 mm2 ToF SiPM detectors with different readout schemes, Frontiers in Physics 11 (2023) 1–9, 1050234.
[21] M. Wang, Y. Wang, Q. Cao, L. Wang, J. Kuang, Y. Xiao, Comparison of three pre-amplifier circuits for time readout of SiPM in TOF-PET detectors, in: 2019 IEEE International Symposium on Circuits and Systems (ISCAS), 2019, pp. 1–5.
[22] C. Piemonte, F. Acerbi, A. Ferri, A. Gola, G. Paternoster, V. Regazzoni, G. Zappala, N. Zorzi, Performance of NUV-HD silicon photomultiplier technology, IEEE Trans. Electron. Dev. 63 (2016) 1111–1116.
[23] F. Monrabal, et al., The NEXT white (NEW) detector, J. Instrum. 13 (2018) 1–28.
[24] I.e. a. Fleck, Handbook of Particle Detection and Imaging, Springer, Cham, 2021.
[25] P. Zydron, M. Kuniewski, L. Fuśnik, Comparison of pseudorandom white-noise generators used as signal source for wideband analysis of transformer windings impedance, in: 9th International Scientific Symposium on Electrical Power Engineering (ELEKTROENERGETIKA), 2017, pp. 1–5.
[26] J. Weber, Oscilloscope Probe Circuits, Prentice Hall, Beaverton, 1969.
[27] H.J. Johnson, M. Graham, High-Speed Digital Design: a Handbook of Black Magic, Prentice Hall, Englewood Cliff, 1993.
[28] M. Romer, S. Murray, J. Schmitz, S. Balkır, M. Hoffman, A low-power analog front-end amplifier for SiPM based radiation detectors, Physics Research Section A: Accelerators, Spectrometers, Detectors and Associated Equipment 1048 (2023) 1–15.
[29] P. Bérard, M. Couture, F. Laforce, B. Fong, H. Dautet, Characterization of a SiPM dedicated at analytical, life science and medical imaging, Proceedings Volume 8621, Optical Components and Materials X (2013) 1–10.
[30] F. Scheuch, D. andT. Hebbeker, C. Heidemann, M. Merschmeyer, Electrical characterization and simulation of SiPMs, Nucl. Instrum. Methods Phys. Res. 787 (2015) 340–343.
[31] D. Marano, G. Bonanno, S. Garozzo, A. Grillo, G. Romeo, A new simple and effective procedure for SiPM electrical parameter extraction, IEEE Sens. J. 16 (2016) 3620–3626.
[32] Y. Zou, F. Villa, D. Bronzi, S. Tisa, A. Tosi, F. Zappa, Planar CMOS analog SiPMs: design, modeling, and characterization, J. Mod. Opt. 62 (2015) 1693–1702.
[33] D. Fink, R. Mirzoyan, M. Teshima, O. Reimann, Measurement and modeling of silicon photomultiplier devices by means of s-parameter techniques, in: 2014 IEEE Nuclear Science Symposium and Medical Imaging Conference, NSS/MIC), 2014, pp. 1–4.